Slabs in the lower mantle and their modulation of plume formation

Eh Tan and Michael Gurnis

Seismological Laboratory, California Institute of Technology, Pasadena, California 91125, USA
(tan2@gps.caltech.edu)

Lijie Han

Seismological Laboratory, California Institute of Technology, Pasadena, California 91125, USA

Now at Earth Sciences Division, Lawrence Berkeley National Laboratory, Berkeley, California 94720, USA

[1] Numerical mantle convection models indicate that subducting slabs can reach the core-mantle boundary (CMB) for a wide range of assumed material properties and plate tectonic histories. An increase in lower mantle viscosity, a phase transition at 660 km depth, depth-dependent thermal expansivity, and depth-dependent thermal diffusivity do not preclude model slabs from reaching the CMB. We find that ancient slabs could be associated with lateral temperature anomalies ∼500°C cooler than ambient mantle. Plausible increases of thermal conductivity with depth will not cause slabs to diffuse away. Regional spherical models with actual plate evolutionary models show that slabs are unlikely to be continuous from the upper mantle to the CMB, even for radially simple mantle structures. The observation from tomography showing only a few continuous slab-like features from the surface to the CMB may be a result of complex plate kinematics, not mantle layering. There are important consequences of deeply penetrating slabs. Our models show that plumes preferentially develop on the edge of slabs. In areas on the CMB free of slabs, plume formation and eruption are expected to be frequent while the basal thermal boundary layer would be thin. However, in areas beneath slabs, the basal thermal boundary layer would be thicker and plume formation infrequent. Beneath slabs, a substantial amount of hot mantle can be trapped over long periods of time, leading to "mega-plume" formation. We predict that patches of low seismic velocity may be found beneath large-scale high seismic velocity structures at the core-mantle boundary. We find that the location, buoyancy, and geochemistry of mega-plumes will differ from those plumes forming at the edge of slabs. Various geophysical and geochemical implications of this finding are discussed.

1. Introduction

[2] Several geophysical observations suggest that slabs penetrate the 660-km seismic discontinuity and descend into the lower mantle. Global tomography models show that some continuous high seismic velocity anomalies extend from active subduction zones to a depth of at least 2000 km [*Grand et al.*, 1997; *van der Hilst et al.*, 1997]. Beneath Japan (Figure 1) and the Caribbean, high seismic velocity anomalies extend nearly continuously from the upper mantle to the very base of the mantle. The spatial distribution of high seismic velocity anomalies in the deep mantle correlates with the position of past subduction [*Richards and Engebretson*, 1992]. However, seismic tomography generally shows that slab continuity from the upper mantle to the CMB is variable, with substantial down dip and along strike variations [*Megnin and Romanowicz*, 2000; *Ritsema and van Heijst*, 2000]. In addition to tomography, other arguments have been advanced suggesting that flow associated with plates penetrates deeply into the lower mantle [*Richards and Engebretson*, 1992] For example, the occurrence of positive geoid and gravity anomalies over subduction zones is most consistent with penetration of slabs into the lower mantle [*Hager*, 1984]. In addition, if the mantle were perfectly layered with a thermal boundary layer (TBL) at 660 km depth, robust buoyant upwellings would produce asymmetrical bathymetry at mid-ocean ridges, which are not observed [*Davies*, 1989].

[3] Some geochemical arguments are also consistent with deeply penetrating slabs. Oceanic island basalts (OIBs) have a wide spectrum of isotopic heterogeneity. The origin of the heterogeneity is attributed to different reservoirs in the deep mantle [*Hofmann*, 1997]. One reservoir sampled by HIMU OIB ("high μ"; μ = $^{238}U/^{204}Pb$) has the highest $^{206}Pb/^{204}Pb$, $^{207}Pb/^{204}Pb$, and $^{208}Pb/^{204}Pb$ and the lowest $^{87}Sr/^{86}Sr$ of any OIB. The high Pb ratios indicate enrichment in U and Th in the HIMU source, while the low Sr ratio indicates depletion in Rb. One potential source of the HIMU reservoir is oceanic crust that has been returned to the deep mantle during subduction [*Hofmann and White*, 1982]. The high Pb ratios and low Sr ratio of HIMU are inherited from the high U and low Rb in the oceanic crust.

[4] Although seismic tomography models provide evidence that some slabs penetrate into the lower mantle, it is not clear that they penetrate to the CMB. There are several factors that might hinder and delay slab decent, leading to substantial warming of slabs before reaching the CMB. In a mantle with a highly viscous lower mantle and a decreasing thermal expansivity with depth, slabs would take a longer time to descend through the lower mantle, perhaps long enough for a slab to thermally dissipate. The radioactive heating in the mantle and slab, although small, might have some influence in the limit of long descent times. Furthermore, the thermal conductivity may increase with depth [*Hofmeister*, 1999] and potentially diminish the temperature anomaly in the slab [*Hauck et al.*, 1999]. Applying these various effects in mantle convection models, we explore under what conditions a slab can survive as a distinct thermal and mechanical entity before reaching the CMB.

[5] On the other hand, assuming that slabs can indeed reach the CMB, they are likely to have a profound influence on the dynamics near the CMB. Regions, called ultra-low velocity zones (ULVZs), with reduction of *P*- and *S*-wave velocities over 10%, are observed at the CMB [*Garnero and Helmberger*, 1996; *Vidale and Hedlin*, 1998; *Ni and Helmberger*, 2001]. Plumes, presumably emanating from a TBL, are putatively rooted at the CMB. The interaction of slabs with ULVZs and plume roots might influence their geographical location.

[6] Three types of dynamic models are presented in this paper. First, large-scale two-dimensional (2-D) cylindrical models with depth-dependent material properties, meant to simulate flow through the whole mantle, were formulated to show under what conditions slabs could reach the CMB. Second, 3-D spherical models with imposed plate evolution were formulated to explore the morphology of slabs in the presence of realistic evolution of surface plates. Last, high-resolution, fine-scale, 2-D
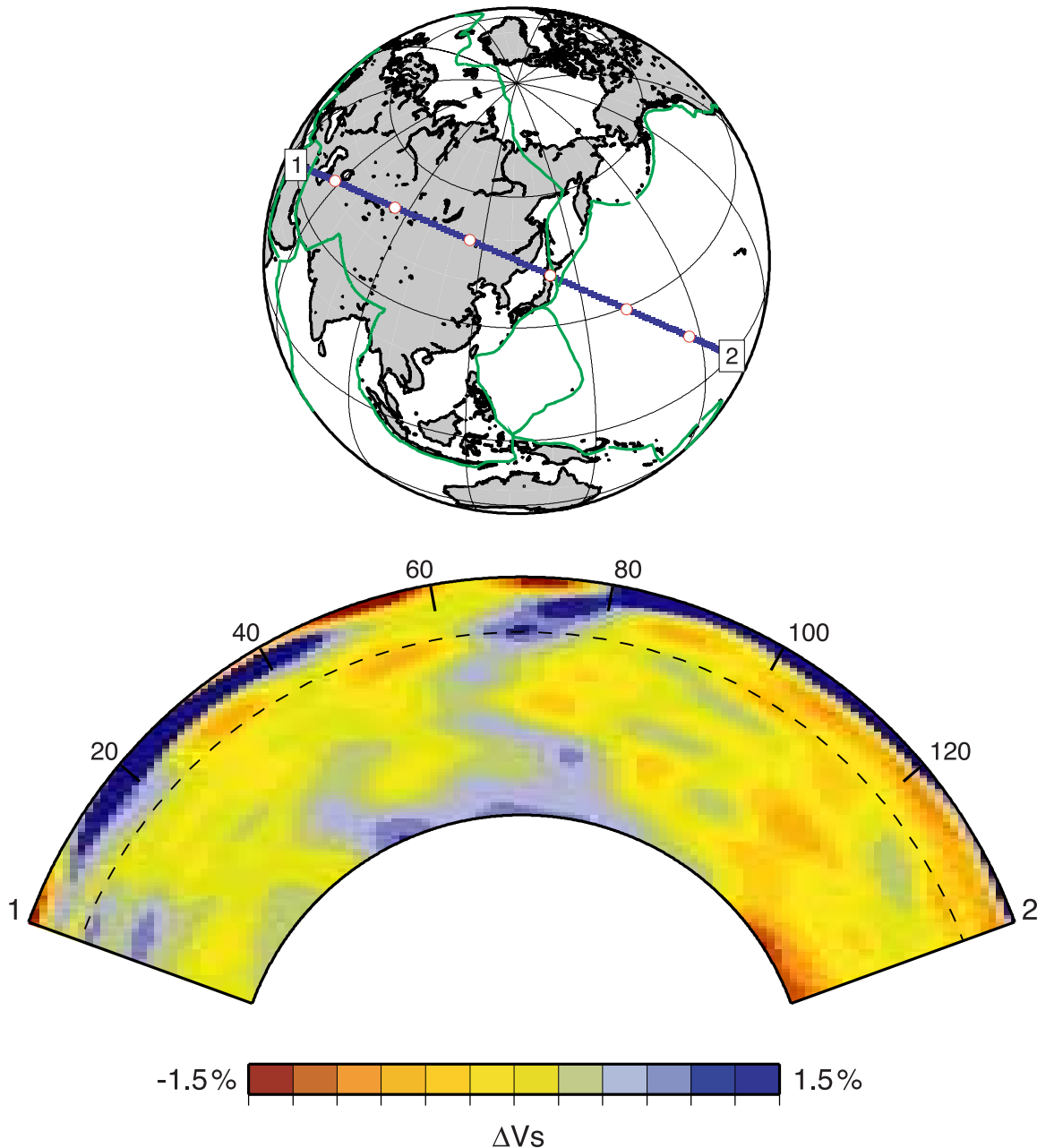
Figure 1. Tomography model S20RTS across Japan subduction zone [*Ritsema and van Heijst*, 2000]. The continuous high seismic velocity anomaly extending from the subduction zone to the CMB is most consistent with subduction of oceanic lithosphere into the lower mantle, clear down to the core mantle boundary.

Cartesian models were formulated to investigate the evolution of slabs near the CMB. Aspects of the formulation common to all of the models will first be described, followed by specified model characteristics and results. Various geophysical and geochemical implications are then considered. Since none of the models include chemical varia-tion, when we refer to "slab", we mean "cold anomaly".

2. Method

[7] The numerical calculations were performed by solving the nondimensional conservation equations

of mass, momentum, and energy using the Boussinesq approximation. The continuity (mass conservation) equation is (except where indicated, all quantities are nondimensional):

$$\nabla \cdot u = 0 \tag{1}$$

where u is the velocity. The momentum equation for a fluid with an infinite Prandtl number is:

$$\nabla \cdot (\eta(r, T)\nabla u) = -\nabla p + (\alpha(r)R_a T - R_b \Gamma)e_r = 0 \tag{2}$$

where η is the dynamic viscosity, p is the dynamic pressure, α is the thermal expansivity, R_a is the thermal Rayleigh number, R_b is the Rayleigh number associated with the density jump across a phase change, Γ is the phase change function, T is the temperature, r is the radius, and e_r is the unit vector in the radial direction. The energy equation is:

$$\frac{\partial T}{\partial t} = -u \cdot \nabla T + \nabla \cdot (\kappa(r)\nabla T) + H \tag{3}$$

where κ is the thermal diffusivity, H is the internal heating number, and t is time. Γ is defined as:

$$\Gamma = \frac{1}{2}\left(1 + \tanh\left(\frac{1 - r - d_{ph} - \gamma(T - T_{ph})}{w_{ph}}\right)\right) \tag{4}$$

where d_{ph} and T_{ph} are the ambient depth and temperature of a phase change, γ is the Clapeyron slope of a phase change, and w_{ph} is the width of a phase transition. The nondimensional Rayleigh numbers, R_a and R_b, are defined in terms of dimensional quantities:

$$R_a = \frac{\rho_0 g \alpha_0 \Delta T \ R_0^3}{\kappa_0 \ \eta_0} \tag{5}$$

$$R_b = \frac{\Delta\rho_{ph} g \ R_0^3}{\kappa_0 \ \eta_0} \tag{6}$$

where ρ_0 is the reference density, g is the gravitational acceleration, α_0 is the reference thermal expansivity, ΔT is the temperature increase across the mantle, R_0 is the scale height of the domain, κ_0 is the reference thermal diffusivity, η_0 is the reference viscosity, and $\Delta\rho_{ph}$ is the density jump across a phase change. The functional forms of material properties, α, κ and η, are different in the large-scale and fine-

Table 1. Values of Parameters Used in Large-Scale Models (2-D)

Symbol	Value
ρ_0	4000 kg/m^3
g	10 m/s^2
ΔT	2900 K
R_0	6371 km
α_0	1.53×10^{-5} K^{-1}
κ_0	10^{-6} m^2/s
η_0	5.57×10^{21} Pa · s
$\Delta\rho_{ph}$	340 kg/m^3
w_{ph}	5.49×10^{-3}
d_{ph}	0.895
T_{ph}	0.5
γ	-0.0398
R_a	7.239×10^7
R_b	1.383×10^8

scale models, and will be given below along with the boundary and initial conditions.

2.1. Large-Scale Model (2-D)

[8] A series of 2-D models of thermal convection in a cylindrical geometry with imposed plate kinematics were computed to investigate the evolution of subduction from the surface to the CMB. We followed the finite element method of *Sidorin and Gurnis* [1998]. The values of all parameters in equations (4)–(6) are listed in Table 1. In this set of models, the material properties, α, κ and η, are depth-dependent.

[9] At higher pressure, it requires more energy to expand or compress a mineral. So, thermal expansivity decreases with depth. This high pressure behavior has been determined experimentally for perovskite and magnesiowüstite [*Wang et al.*, 1994; *Chopelas*, 1996] and is well represented by the nondimensional equation:

$$\alpha(r) = \frac{\alpha_s}{1 + a(1 - r)^b} \tag{7}$$

where α_s = 2.93 is the nondimensional thermal expansivity at the surface, a = 10.5 and b = 0.85 are fitting constants. This equation is an empirical fit to the theoretical values of thermal expansivity along a mantle adiabat [*Sidorin and Gurnis*, 1998]. The dimensional value of reference thermal expansivity, α_0, is chosen so that the volume average (geometric mean) of α is equal to 1.

[10] Most radial viscosity profiles inverted from the geoid and postglacial rebound have a one to two orders of magnitude increase across the 660-km discontinuity [*Hager et al.*, 1985; *Mitrovica and Forte*, 1997; *Lambeck et al.*, 1998]. In order to include this effect, we used a modified Arrhenius law:

$$\eta(r, T) = \eta^* \exp\left(\frac{c_1}{c_2 + T} - \frac{c_1}{c_2 + T_m}\right) \quad (8)$$

where $\eta^* = 0.18$ in the upper mantle and 1.8 in the lower mantle, $T_m = 0.5$ is the nondimensional temperature of ambient mantle, $c_1 = 17.22$, and $c_2 = 0.64$. A high viscosity cutoff of 10^3 is used. These parameters give three orders of magnitude variation in viscosity across the top TBL, one order of magnitude viscosity jump across the 660-km discontinuity, and another two orders of magnitude variation across the bottom TBL. The dimensional value of reference viscosity, η_0, is chosen so that the volume average (geometric mean) of η is equal to 1.

[11] The thermal diffusivity, proportional to the thermal conductivity, may increase with depth (decrease with r) [*Hofmeister*, 1999]. Because the precise relation between κ and r is unknown, a simple implementation is used:

$$\kappa(r) = 1 + \delta_\kappa f(r) \quad (9)$$

where δ_κ is a model parameter that controls the variation of thermal diffusivity across the mantle, and $f(r)$ is a stepwise decreasing function with value from 1 to 0. This formula represents a 10-layer mantle, with constant thermal diffusivity in each layer. The dimensional value of reference thermal diffusivity, κ_0, is chosen to be the surface thermal diffusivity.

[12] The phase change parameters are chosen to be consistent with seismological observations and high-pressure experiments. From the amplitudes of reflected seismic phases off the 660-km discontinuity, the density jump across the discontinuity is estimated as $4 \sim 6\%$ [*Shearer and Flanagan*, 1999], substantially below the value of 9.3% in PREM [*Dziewonski and Anderson*, 1981]. The Clapeyron slope of spinel dissociation has been determined experimentally and falls between -2.8 MPa/K [*Ito and Takahashi*, 1989] to -3 ± 1 MPa/K [*Akaogi and Ito*, 1993a]. To infer the minimum temperature anomalies of slabs when they reach the CMB, we over-estimated the influence of the post-spinel phase change. We used phase change parameters corresponding to an ambient depth of 660 km with Clapeyron slope of -3.5 MPa/K and a density jump of 8.5%.

[13] The computations were performed within a half annulus (Figure 2) in a cylindrical coordinate system (r, φ), where the inner radius corresponds to the CMB and the outer radius corresponds to the surface of the Earth. This domain is divided into 400 elements in the φ direction and 100 elements in the r direction. The mesh was refined vertically and horizontally to increase the resolution in the TBLs and in the area of subduction, with a minimum grid spacing of 15 km. Reflecting boundary conditions were used for both sidewalls. At the bottom, free-slip velocity boundary conditions were used and temperature was kept constant at 1. At the top, plates were simulated by imposing piecewise constant velocity boundary conditions. There were 3 plates along the top. Each had different velocity and temperature boundary conditions. These plates were, from left to right, the oceanic plate, a plate within the back-arc basin, and the overriding plate. The back-arc basin was introduced to initiate subduction and to prevent the slab from being sucked up under the overriding plate [*Christensen*, 1996]. The thickness of the oceanic plate progressively increased from the ridge (left margin) to the trench (right margin) and was concordant with the plate age A_{OC}. The mantle was initially isothermal, with $T_m = 0.5$, except for the bottom TBL. These calculations were meant to model an oceanic plate descending through an initially isothermal mantle with a hot TBL at the CMB. In one model, a different initial condition is used; the slab descends through a mantle with preexisting convection. All models were integrated forward in time until slabs reached and spread along the top of the CMB.

2.2. Large-Scale Model (3-D)

[14] With a somewhat simpler mantle structure, we explored the influence of a realistic evolving plate
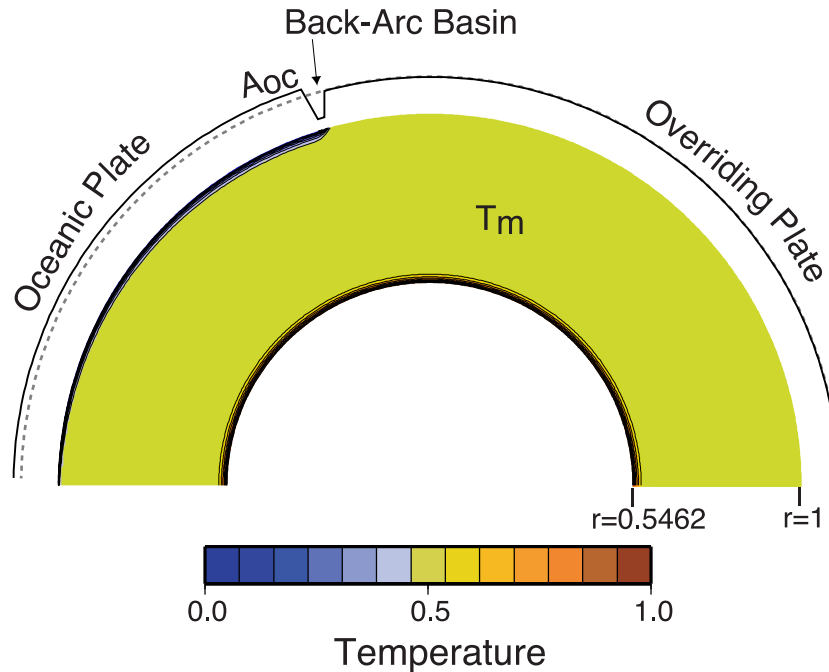
Figure 2. Initial configuration of 2-D large-scale models. There are three tectonic plates at the top with different velocity and temperature boundary conditions. These plates are, from left to right, the oceanic plate (OC), a plate within the back-arc basin (overshooting plate, OS), and the overriding plate (OR). The velocities of these plates are $V_{OR} = -0.25$ cm/yr, $V_{OS} = -5V_{OC}$, and V_{OC} is a model parameter. The plate boundaries between OC and OS and that between OR and OS both have the same velocity as V_{OR}. The temperature on the top surface is $T_{OS} = T_{OR} = 0.5$ and $T_{OC} = 0$. The age of the oceanic plate at the trench, A_{OC}, is another model parameter. On the bottom surface, free-slip velocity boundary conditions are used and temperature is 1. Reflection boundary conditions are used for both sidewalls. The mantle has an initial uniform temperature $T_m = 0.5$.

boundary on slab morphology. Using CitcomS, a spherical finite element code [*Moresi et al.*, 2000], we set up a regional model, which encompassed the evolution of the western boundary of North America from the Cretaceous to the present.

[15] The mantle was purely heated from below and was initially isothermal at $T_m = 1$. This configuration only resulted in a small amount of basal heating such that no plumes formed. There was one phase change in the model, representing the 660-km discontinuity. The phase change parameters corresponded to an 8.5% density jump. The values of all parameters in equations (4)–(6) are listed in Table 2. Both the thermal expansivity and thermal diffusivity were constant through the mantle, while the viscosity was temperature- and depth-dependent. The temperature-dependent part of viscosity was expressed as equation (8). The mantle was divided into four layers with a different set of constants (η^*, c_1, c_2) in each layer (Table 3). The

Clapeyron slopes and viscosity of lower mantle are varied in different models.

[16] The model domain was 220° to 310°E and 0° to 45°N, extending from surface to the CMB. On these four vertical boundaries, the shear stress was

Table 2. Values of Parameters Used in Large-Scale Models (3-D)

Symbol	Value
ρ_0	3500 kg/m^3
g	10 m/s^2
ΔT	1500 K
R_0	6371 km
α_0	2×10^{-5} K^{-1}
κ_0	10^{-6} m^2/s
η_0	2×10^{21} Pa · s
$\Delta\rho_{ph}$	340 kg/m^3
w_{ph}	5.8×10^{-3}
d_{ph}	0.875
T_{ph}	1
R_a	1.357×10^7
R_b	3.846×10^8

Table 3. Viscosity in Each Layer Used in Large-Scale Models (3-D)

Depth, km	Viscosity, Pa · s	Viscosity Variation
0–90	2×10^{23}	100
90–410	4×10^{18}	200
410–660	4×10^{21}	10
660–CMB	model dependent	10

set to zero. The bottom surface had free-slip and isothermal boundary conditions, with temperature kept at T_m. The top surface, like the 2-D large-scale model just described, had imposed velocity boundary conditions. The top surface had a constant temperature $T = 0$.

[17] Three different plate evolutionary models were used (Table 4). The coordinates of plate boundaries and poles of rotations are from *Lithgow-Bertelloni and Richards* [1998]. For the first evolutionary model (used for NA1-NA3), the calculations started at 119 Ma with an evolving set of plate motions. Since this model started with an isothermal mantle, subduction essentially initiated at the western boundary of the North American plate at 119 Ma. In a second evolutionary model (used only for NA4), the plate evolution from 119 Ma to the present was identical to that used for NA1-NA3. However, prior to 119 Ma, we continuously imposed the 119 Ma plate reconstruction for 70 Myr; since the model started with an isothermal mantle, subduction essentially initiated at 189 Ma along the western boundary of the North American plate. Finally, in a third evolutionary model (used only for NA5), we incorporated evolving plate boundaries back to 150 Ma while also incorporating the distributed (nonplate tectonic) strain of western United States from 20 Ma to the present using the reconstructions in *Atwater and Stock* [1998].

2.3. Fine-Scale Model

[18] Last, we formulated a series of fine-scale 2-D Cartesian models to investigate the interaction between a slab and CMB using the finite element program ConMan [*King et al.*, 1990]. The models had a dimension of 3000 km in width and 1500 km in height and were computed on a mesh with 300 elements in the horizontal direction and 150 ele-

ments in the vertical direction. The grid size is uneven, with a minimum grid spacing of 5 km. For this study, the dynamics were determined by the initial conditions of a slab, which consisted of slab temperature, thickness, and viscosity. A slab with an initial length of 1250 km, but variable thickness, W_s, and temperature, T_s, laid horizontally 80 km above the CMB (Figure 3). The models initially started with a TBL along the bottom with a uniform mantle temperature ($T_m = 0.5$). Reflecting boundary conditions were used for both sidewalls. At the bottom, free-slip boundary conditions were used and the temperature was kept constant at 1. At the top, permeable boundary conditions were used. These boundary conditions allow plumes to ascend and escape from the calculation domain while the continuity equation ensured that the total volume of the domain was conserved.

[19] The material properties used here are different from those used in the large-scale models. Because the depth variation is half of the value used in the large-scale models, we used a constant thermal expansivity and diffusivity. The viscosity is only temperature-dependent, and a two-step rheology is used:

$$\eta(T) = \begin{cases} 10^{-6(T-T_m)} & \text{for } T > T_m \\ 10^{-\delta_\eta(T-T_m)/(T_s-T_m)} & \text{for } T < T_m \end{cases} \quad (10)$$

where δ_η is a parameter controlling the viscosity variation in the slab. This relation allows the initial viscosity contrast between the slab and mantle to be held constant while changing the initial slab temperature. This allows us to deconvolve the influence of slab viscosity from its temperature during its subsequent evolution. The temperature dependence of viscosity gives δ_η orders of magnitude variation in viscosity between the slab and

Table 4. Large-Scale (3-D) Models

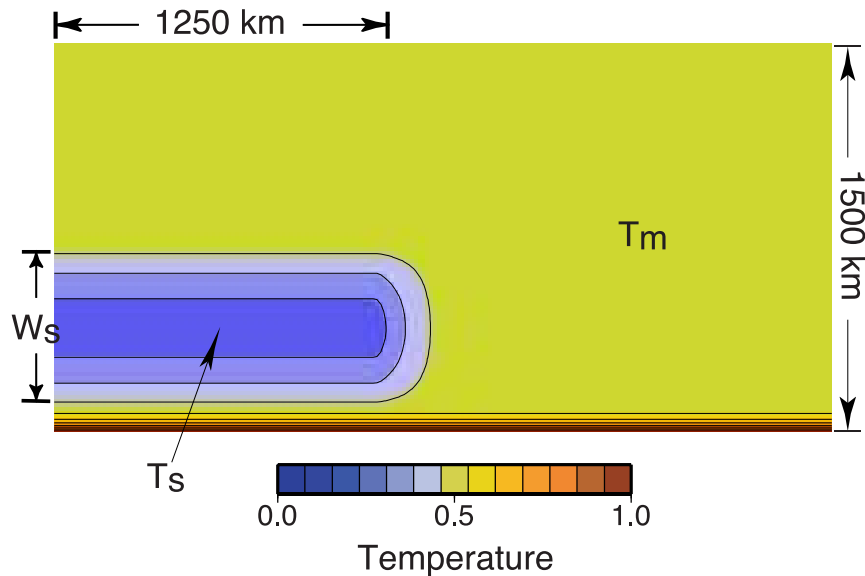| Model	Clapeyron Slope	Lower Mantle Viscosity, Pa · s	Plate Evolutionary Model (See Text)
NA1	3.5 MPa/K	2×10^{22}	Model 1
NA2	1.75 MPa/K	2×10^{22}	Model 1
NA3	1.75 MPa/K	4×10^{22}	Model 1
NA4	1.75 MPa/K	2×10^{22}	Model 2
NA5	1.75 MPa/K	2×10^{22}	Model 3

Figure 3. Initial configuration of fine-scale models. A slab with a constant length, 1250 km, but variable thickness, W_s, and temperature, T_s, laid horizontally 80 km above the CMB. A TBL with a temperature profile as if developed for 100 Myr was imposed along the bottom. The mantle was initially at a uniform temperature, T_m, of 0.5.

mantle and 3 orders of magnitude variations between the mantle and CMB. We did not consider internal heating because basal heating dominates the dynamics of this problem. The values of all parameters in equations (4)–(6) are listed in Table 5.

3. Results

3.1. Large-Scale Model (2-D)

[20] For different models, we varied oceanic plate velocity and age (labeled with V), thermal diffusivity (labeled with K), internal heating (labeled with H), and the presence of a 660-km phase change (labeled with P). The parameters and results of models are listed in Table 6.

[21] For all the models explored, slabs consistently descend to the CMB with substantial temperature anomalies. The animation from model P2 demonstrates the typical history of a slab (Animation 1; Figure 4). In this model, the position of subduction rolls back to the left, governed by the boundary conditions, and the slab directly penetrates the 660-km phase change. The slab only thickens slightly as it enters the more viscous and dense lower mantle. The near vertical dip of the slab and the simplicity of the initial and boundary conditions result in a continuous, unbroken slab. The slab,

while descending through the lower mantle, induces a down-welling flow and depresses the thickness of the underlying TBL. This flow pushes hot mantle aside (left inset of Animation 1) so that the neighboring TBL thickens, even when the slab is hundreds of kilometers above the CMB (Figure 4a). The thickening TBL is prone to instability and new plumes form (right inset of Animation 1). As the tip of the slab reaches the CMB, the slab slides horizontally and sweeps hot mantle aside, including the plume root, until the slab comes to a rest on the CMB (Figure 4b). Therefore, in these 2-D models, there is always a plume on the tip of the slab. Similar phenomenon has been noticed in other studies [*Weinstein et al.*, 1989; *Lenardic*

Table 5. Values of Parameters Used in Fine-Scale Models

Symbol	Value
ρ_0	5000 km/m³
g	10 m/s²
ΔT	2900 K
R_0	1500 km
α_0	10^5 K⁻¹
κ_0	10^{-6} m²/s
η_0	10^{22} Pa · s
R_a	4.89×10^5
R_b	0

Table 6. Results of Large-Scale Models (2-D)

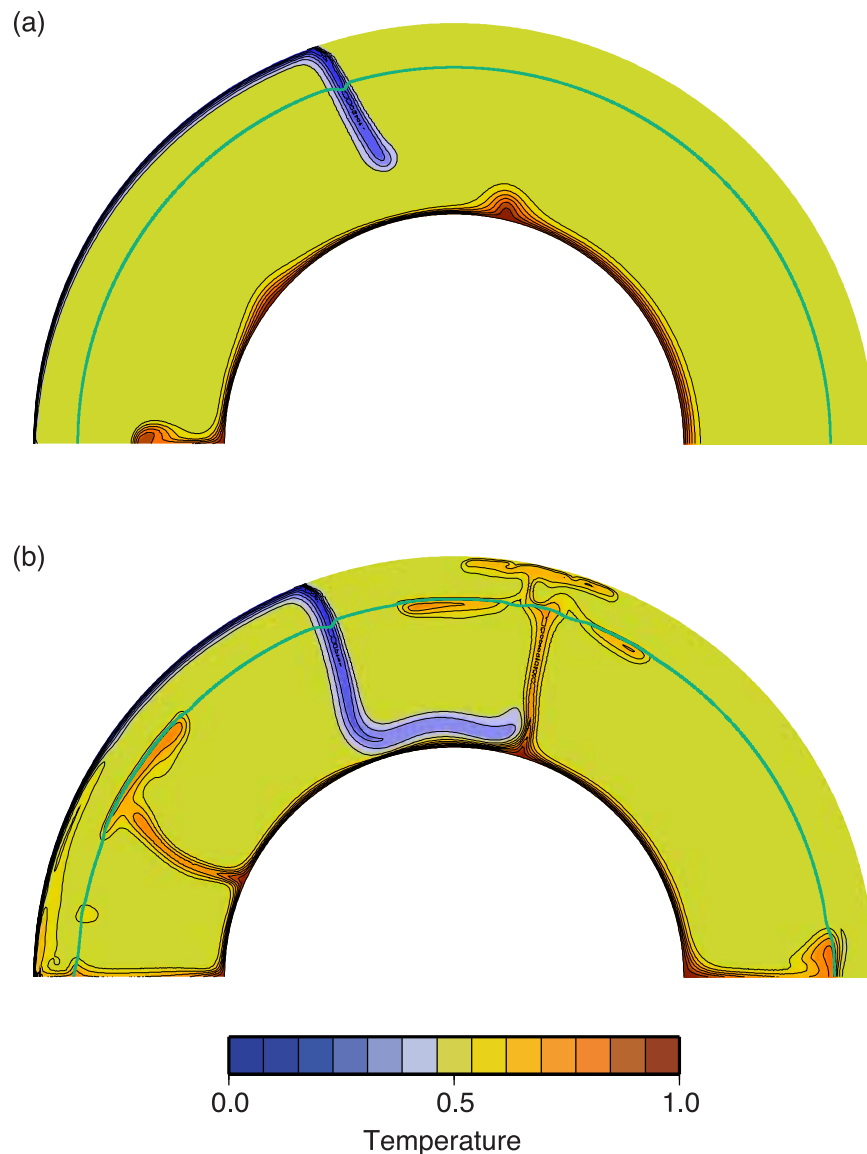| Model	V1	V2	V3	K2	K3	K4	K8	H1	P1	P2
V_{OC} (cm/yr)	5	10	2.5	5	5	5	5	5	5	5
A_{OC} (Myr)	130	65	260	130	130	130	130	130	130	130
δ_κ	0	0	0	1	2	3	7	0	0	2
H	0	0	0	0	0	0	0	18	0	18
Phase change	No	No	No	No	No	No	No	No	Yes	Yes
W_s (km)	498	459	546	543	543	543	543	467	645	546
T_s	0.30	0.31	0.31	0.31	0.34	0.37	0.40	0.30	0.28	0.34
Temperature anomaly $(T_m - T_s)\Delta T$ (°C)	580	551	551	551	464	377	290	580	638	464

Figure 4. Temperature fields of Model P2. The green lines mark the 660-km phase boundary. (a) When the slab descends through the lower mantle, it induces a down-welling flow. This flow depresses the thickness of the TBL directly beneath the slab and pushes hot materials aside, thus thickening the neighbored TBL, even when the slab is still relatively distant from the CMB. The thickened TBL is prone to instability and initiates the growth of a new plume. (b) As the tip of the slab reaches the CMB, the slab slides horizontally while sweeping hot material aside (including the plume root).
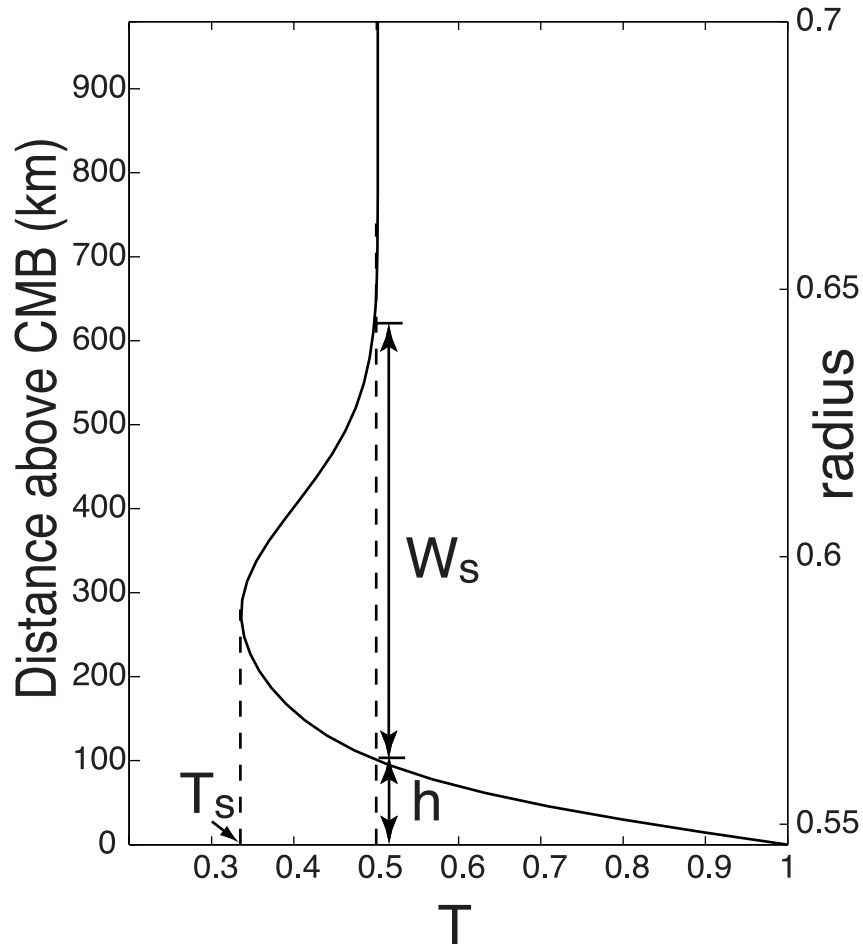
Figure 5. The temperature profile across the slab in the final step of model P2. T_s and W_s are the temperature and thickness of the slab. The h is the height of the slab above the CMB.

and Kaula, 1994; Lowman and Jarvis, 1996; Zhong and Gurnis, 1997; Sidorin et al., 1999]. The slab also folds and buckles as it approach the CMB. Even with trench rollback, slabs near the CMB can be found under both the overriding and subducting plates. It also appears that some hot mantle can become trapped beneath the cold slab.

[22] The temperature and thickness of the slab, T_s and W_s, are measured by taking a temperature profile (Figure 5) near the midpoint of the flat-lying slab, where the horizontal temperature variation is small. T_s is defined as the minimum temperature in the profile, and W_s is defined as the vertical extent of the slab (the region with $T < T_m$). The height of the slab above the CMB, h, is defined as the distance between the base of the slab (where $T = T_m$) and the CMB. The values of T_s and W_s for all

models are given in Table 6. We find that slabs usually lay 50–80 km above the CMB and are associated with a temperature anomaly of 300° to 600°C while having thicknesses of 450 to 650 km.

[23] The results show that T_s and W_s do not change substantially in spite of the variation in the plate age. This result is surprising, since the oceanic plate thickness is proportional to the square root of the plate age, according to the half-space cooling-plate model. Model V3 has an oceanic plate four times older than model V2, thus the plate is twice as thick on the surface, but the slab in V3 is only 16% thicker and is as cold as the slab in V2. This result can be explained by the compensating effect of different plate velocities. When slabs reach the lower mantle, the vertical descent of slabs decrease and slabs thicken in response to the increase of

viscous resistance. This advective thickening may have been observed in several subduction zones [*Creager and Jordan*, 1986; *Fischer et al.*, 1991; *Ding and Grand*, 1994; *Pankow and Lay*, 1999]. A fast moving slab may experience more advective thickening, so it gets more insulated and heats less than a slow-moving slab. On the other hand, a slab attached to a fast moving plate spends less time in the mantle before reaching the CMB and heats less.

[24] Comparing model V1 and H1, we find that internal heating does not increase the temperature inside the slab, consistent with order of magnitude estimates. If the mantle has an internal heating number $H = 18$, equivalent to a heat generation rate of 1.6×10^{-12} W/kg, the temperature of the slab will increase by 10°C after 250 Myr. If the chondritic value of heat generation rate (5.1×10^{-12} W/kg) is used instead, the temperature increase will be 32°C. This temperature increase is negligible. Although we use a uniform H for the mantle and slab, this result suggests that using a larger H for the slab, representing a higher concentration of radioactive elements in the oceanic crust, would not change the slab temperature substantially.

[25] The effect of depth-dependent thermal diffusivity can be significant. From model V1, and K2 to K8, the variation of thermal diffusivity, $\delta\eta$, changes from 0 to 7, and the thermal anomalies of slabs decrease as a result. The temperature anomaly of the slab in model K8 is only half of that in model V1, but the slab in model K8 is still 280°C cooler than surrounding mantle. We conclude that an eight-fold or more increase of thermal diffusivity with depth is required to diffusively dissipate the slab before reaching the CMB. The plausible value of $\delta\kappa$ in the mantle will be discussed in a later section.

[26] In our models, the 660-km phase change fails to halt the slab from sinking to the lower mantle, corroborating earlier work by others [*Christensen*, 1995; *Zhong and Gurnis*, 1995; *van Keken and Ballentine*, 1999]. We find that the slab is not obstructed by the phase change and directly penetrates into the lower mantle, possibly due to the near-vertical dip of the slab in our models. If the trench migrated faster, we would expect to get more

time-dependent slab penetration. Although slabs are not halted by the phase change, hot plumes are obstructed from ascending to the upper mantle, at least temporarily [*Davies*, 1995]. Several secondary plumes may form in the upper mantle when the plumes from the CMB collide into the phase boundary and laterally spread out beneath it (Figure 4b).

[27] We found there is always a plume on the tip of the slab, independent of changes in plate kinematics, internal heating, and thermal diffusivity. To determine if this phenomenon was a result of our particular initial conditions, we ran another model with a different history. The model had the same material parameters as model P2, except that the plates were stationary for the first 470 Myrs, after which several plumes developed at the CMB and ascended to the surface. Then, the same kinematic history used in P2 was imposed for 250 Myrs. We find that the slab still sinks to the CMB. When the slab slides along the CMB, it sweeps plumes to the edge of the slab, so the slab still has a plume on the edge. This suggests that plume formation on the edge of a slab is not an artifact of our simple initial conditions.

3.2. Large-Scale Model (3-D)

[28] The plate history in previous 2-D models was simplified considerably from what is found in subduction systems. In previous models, plate and margin velocities did not change over hundreds of millions of years. These time-invariant boundary conditions give continuous slabs extending from the top surface to the CMB (Animation 1; Figure 4). However, plate velocities and boundaries [*Atwater*, 1970; *Ben-Avraham and Uyeda*, 1983] change with time. Therefore, it is possible that we would not find continuous slabs in every subduction zone; in dynamic models with realistic plate histories, it could turn out that continuous slabs are the exception, not the rule. Using a 3-D model with a realistic plate history of North America-Pacific, we explore the influence of time-dependent plate velocities and plate boundaries on slab morphology in the lower mantle. We have not attempted to reproduce mantle structure as seen in the tomography by varying either plate history or mantle rheology.
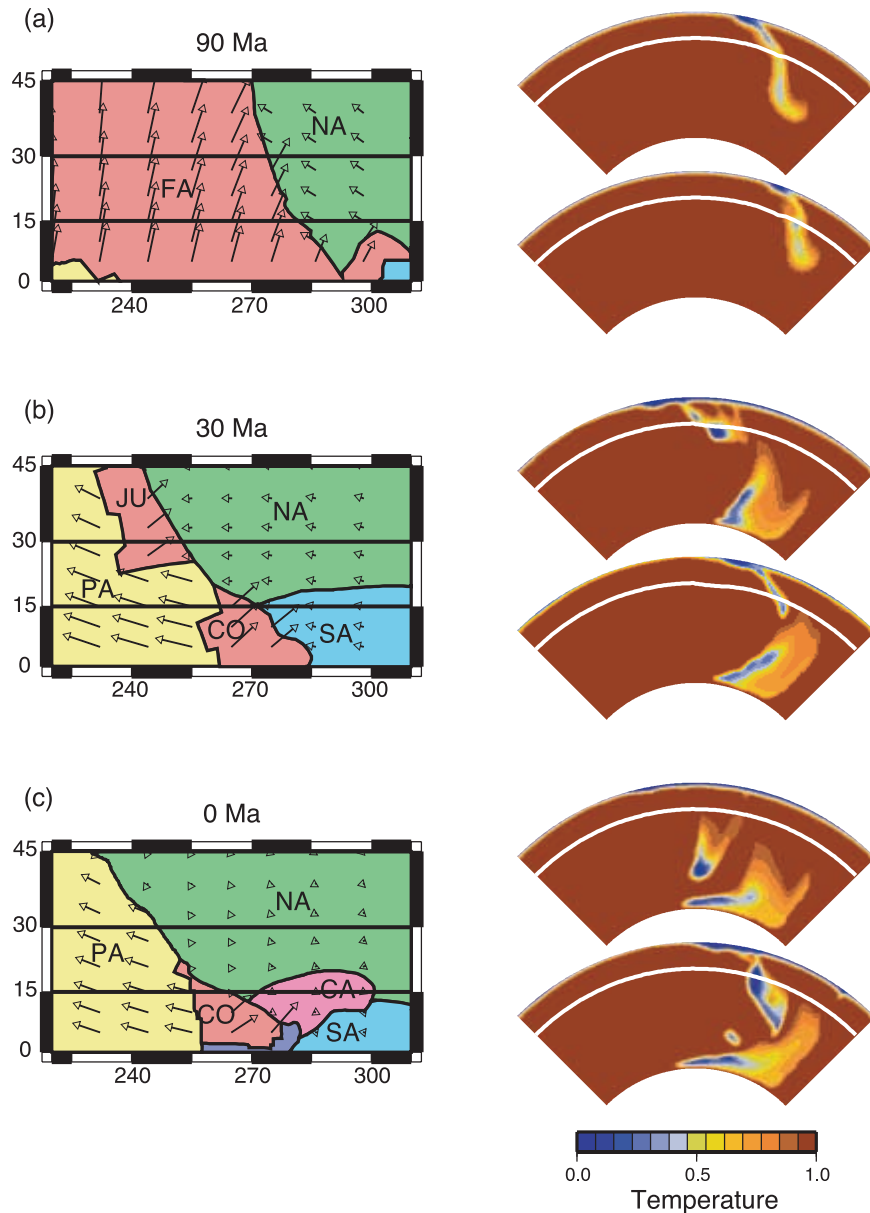
Figure 6. Regional spherical models with the evolution of the North American-Pacific-Farallon plate boundary. The white line is the 660 km discontinuity. (a) Left panel shows the plate configuration at 90 Ma. Right panels are the temperature cross-sections at 30°N (above) and 15°N (below). (b, c) The same as Figure 6a, but at 30 and 0 Ma, respectively. Plate abbreviation: CA, Caribbean; CO, Cocos; FA, Farallon; JU, Juan de Fuca; NA, North America; PA, Pacific; SA, South America.

[29] The evolution of model NA5 is shown in Figure 6 and Animation 2. Since the plate configuration is simple before 85 Ma (similar to the large-scale 2-D models), the slab continuously extends from the surface to mid-mantle (Figure 6a). Between 85 and 75 Ma, the convergence angle between the Farallon and North American plates becomes considerably oblique, so the rate of sub-

duction decreases, resulting in a gap in the continuity of the slab in the mid-mantle at 30 Ma (Figure 6b). The slab is lying flat underneath the over-riding continental plate. This tendency to become flat lying beneath the continent is consistent with earlier 2-D calculations [*Zhong and Gurnis*, 1995] and is caused by the strong suction force. This shallowing of dip is partly a conse-

quence of the trench migration to the west and partly a consequence of the decreasing age of the subducting Farallon plate, as the Farallon-Pacific ridge and Farallon-North American margin converge. Eventually, the ridge and trench coalesce [*Atwater*, 1970]. Since subduction terminates at 30°N after 25 Ma while it continues south of 15°N, slab structure becomes complex. This complexity is particularly evident along strike at 0 Ma (Figure 6c). At 30°N, the slab is completely detached from the surface, and there is no slab in the upper mantle. However, at 15°N, the slab is still attached to the surface. The slab thickness changes significantly at different depths and latitudes and has substantial gaps at mid-mantle depths. Other cases (NA1-NA4), with different variants of plate evolution, phase transition strengths, and lower mantle viscosity, all show complex slab structure. We conclude that slabs are not expected to be continuous between the upper and lower mantle, even in the context of whole mantle convection.

3.3. Fine-Scale Model

[30] Since slabs are associated with large temperature variations, and the viscosity of the hot TBL at the CMB is likely to be small, a model with a high spatial resolution is required to study the long-term evolution of slabs at the CMB. In order to minimize the computational expense, we used fine-scale models (Figure 3) of a small physical domain. These models have initial conditions (slab temperature and thickness) adapted from previous 2-D large-scale models, while ignoring the effect of continuing subduction.

[31] We started with $T_s = 0.275$, corresponding to a temperature anomaly of 650°C, and $W_s = 645$ km. In order to explore the parameter space, we independently varied T_s, W_s, and the viscosity contrast between the slab and mantle, $\delta\eta$. We define two auxiliary parameters, the initial negative buoyancy and the initial stiffness of the slab, B_s and S:

$$B_s = -\int\int_{\text{slab}} (T - T_m)\mathrm{dV} \quad \text{at } t = 0 \qquad (11)$$

$$S = \int\int_{\text{slab}} \log(\eta)\mathrm{dV} \quad \text{at } t = 0 \qquad (12)$$

We find three model outcomes. (1) For thin and less stiff slabs, slabs will heat and dissipate quickly (Animation 3, Figure 7). (2) For thick and stiff slabs, mega-plumes, with unusually large buoyancies, form beneath slabs (Animation 4, Figure 8). (3) For moderately thick and less stiff slabs, plumes with normal buoyancy form beneath slabs. (This third type is essentially a transition between the first two.) We are able to distinguish these outcomes by measuring the eruption time, t_e (defined later), and the plume buoyancy at eruption, $B_e = B(t_e)$. The plume buoyancy is defined as:

$$B(t) = \int_{T>T_m} (T - T_m)\mathrm{dV} \qquad (13)$$

This integral is carried out within a small region near the center of the slab (i.e. left margin of the domain) to avoid contamination from the bottom TBL and plumes in the slab-free area. t_e is the time when the plume buoyancy reaches the maximum. B_e, then, is the maximum plume buoyancy. The results of fine-scale models are listed in Table 7.

[32] The demarcation between these outcomes becomes evident when we look at B_e and t_e in the space of B_s and S (Figure 9). The transition between type-1 and 2 outcomes is roughly delineated by a single line (dashed line in Figure 9). The buoyancy of the mega-plume, B_e, and the eruption time of the mega-plume, t_e, are generally positively correlated, i.e. longer eruption times lead to larger plumes. The general trend is for slabs with larger B_s and S (resulting from colder and thicker slabs, and larger δ_η and thicker slabs, respectively) to lead to larger plumes erupting after longer times. The initial slab stiffness, S, is the major limiting factor since this transition boundary is elongate along the B_s axis. An explanation will be provided below. When B_s and S are both small, the behavior is complex, and no clear boundary can be delineated.

[33] The dynamics of models with type-1 outcomes are considered first. In these models, as a slab warms, its viscosity decreases, and it deforms more easily. The slab starts to spread out, pushes the hot materials aside, and, essentially, its tip blocks the only exit for hot material to escape from beneath
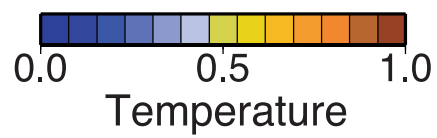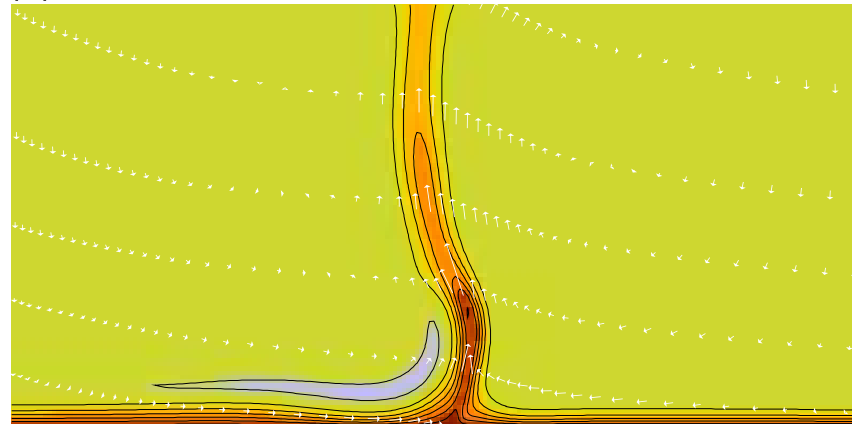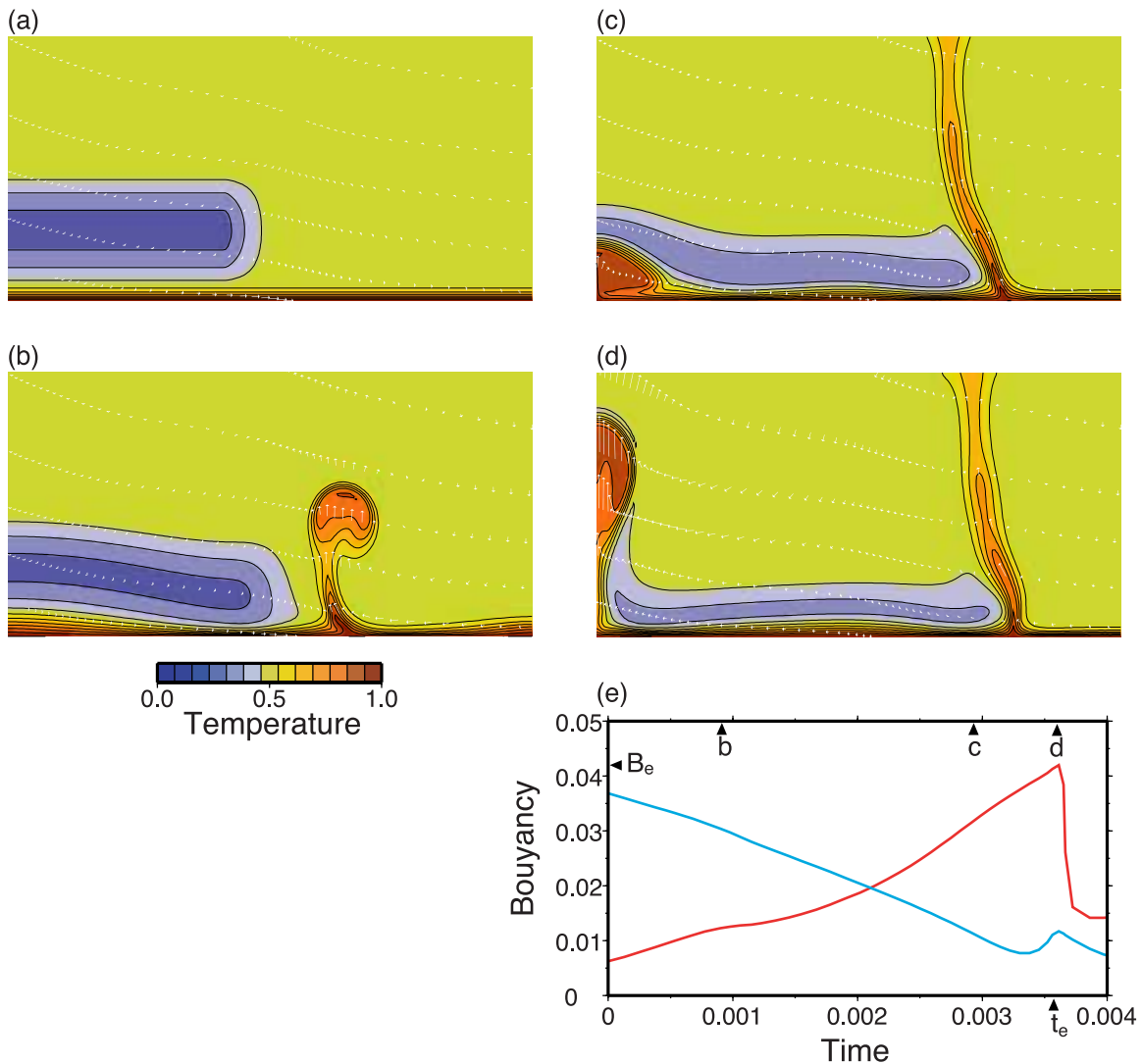
(a)

(b)

(c)
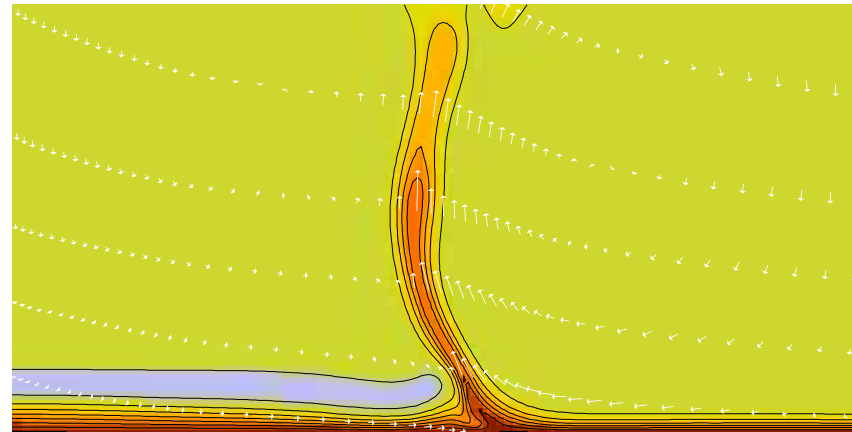
Temperature

Figure 8. Result of model with type-2 outcome (Model F10). (a) Initial condition. (b−d) snapshots of temperature and velocity fields. (e) The buoyancy evolution of the slab and mega-plume. Blue line represents the negative buoyancy of the slab, while the red dashed line represents the positive buoyancy of the hot material. The time of frame Figures 8b, 8c, and 8d is indicated. The eruption time, t_e, of the mega-plume is when the buoyancy of the hot material reaches its maximum, B_e.

the slab. The importance of this blockage will soon become evident. The hot TBL adjacent to the slab is thickened and initiates a plume. For convenience, we will call it an ordinary plume. This plume head ascends through the mantle and is fed by a thin conduit, which continuously drains the hot

mantle near the CMB. The TBL in the slab-free area thins as a result. The TBL beneath the slab is blocked and is not drained by the plume conduit, so it is thicker than the TBL in the slab-free area at this stage (Figure 7b). The thin slab quickly heats, diffuses away, and fails to keep the TBL beneath

Figure 7. (opposite) Result of model with type-1 outcome (Model F3). (a) Initial condition. (b) As the slab warms, the slab tip sinks, pushing hot materials aside, and essentially blocking the only exit for hot material to escape from beneath the slab. The hot TBL adjacent to the slab thickens while a new plume initiates. The TBL beneath the slab is thicker than the TBL in the slab-free area. (c) The thin slab quickly heats, diffuses away, and fails to keep the TBL beneath from being drained. The TBL has uniform thickness after the slab disappears.

Table 7. Results of Fine-Scale Models

Model	F1	F2	F3	F4	F5	F6	F7	F8	F9
W_s (km)	645	332	161	1000	645	645	332	161	322
T_s	0.275	0.275	0.275	0.275	0.431	0.155	0.431	0.431	0.215
δ_η	3	3	3	3	3	3	3	3	3
B_s	0.031	0.015	0.011	0.048	0.009	0.048	0.005	0.002	0.019
S	0.943	0.469	0.233	1.464	0.941	0.944	0.132	0.700	0.470
B_e	0.058	0.040	-	0.082	0.050	0.056	0.048	0.039	0.039
t_e	0.0064	0.0033	-	0.0098	0.0068	0.0064	0.0028	0.0033	0.0035

Model	F10	F11	F12	F13	F14	F15	F16	F17	F18
W_s (km)	645	332	161	1000	645	645	332	161	322
T_s	0.275	0.275	0.275	0.275	0.431	0.155	0.431	0.431	0.215
δ_η	2	2	2	2	2	2	2	2	2
B_s	0.031	0.015	0.011	0.048	0.009	0.048	0.005	0.002	0.019
S	0.629	0.313	0.156	1.976	0.626	0.629	0.085	0.047	0.314
B_e	0.042	0.028	-	0.050	0.056	0.028	0.038	0.044	-
t_e	0.0037	0.0032	-	0.0047	0.0038	0.0038	0.0023	0.0024	-

from being drained. The TBL has uniform thickness after the slab disappears (Figure 7c).

[34] We now consider the dynamics of models that have type-2 outcomes. During the early stage of these models, the dynamics is the same as type-1 outcomes (Figures 8a and 8b). However, the thicker slab survives longer so that a substantial amount of hot mantle has become trapped. With this trapped hot mantle, convection beneath the slab becomes vigorous (Figure 8c). When the trapped mantle accumulates enough buoyancy, it lifts, tilts, and finally breaks through the slab (Figure 8d). This plume can have a buoyancy three times larger than an ordinary plume, hence our term, mega-plume. The buoyancy evolution of the slab and mega-plume is plotted in Figure 8e. The buoyancy of the mega-plume increases with time at the expense of the negative buoyancy of the slab. We note here that most of the reheated slab material becomes incorporated into the mega-plume. The geochemical significance of this will be considered later. When the mega-plume erupts, B_e is six times larger than the negative buoyancy of
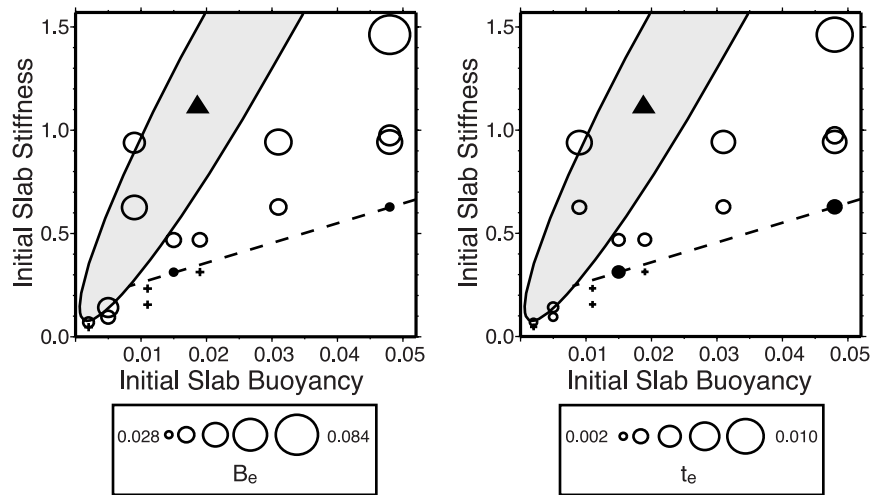

Figure 9. Summary of fine-scale models. Crosses denote models with type-1 outcomes, unfilled circles denote type-2, while solid circles denote type-3. The radii of the circles are proportional to B_e in the left panel and to t_e in the right panel. The transition between type-1 and 2 outcomes are delineated by the dashed line. The solid triangle indicates our best estimate for plausible slab conditions within the mantle, while the shaded ellipse indicates the uncertainty of our estimate.

the remnant slab. This disproportionality suggests that the trapped mega-plume is the result of high slab viscosity, not of high slab density. The sudden increase of the plume's vertical velocity when it escapes the domain, as clearly seen in Animation 4, is an artifact of the boundary condition, because the plume encounters no viscous resistance as it reaches the top boundary. However, this phenomenon occurs after the plume has erupted and moved away from the slab, so there is no evidence that the permeable boundary condition interferes with pre-eruption plume growth.

[35] In models with type-3 outcomes, slabs also traps hot mantle beneath, but plumes breaking through slabs have similar buoyancies to ordinary plumes. These models have larger t_e than some models with type-2 outcomes, indicating that the smaller plumes are not resulting from insufficient time to develop, but from the inability of weaker slabs to hold large plume buoyancies down. We conclude that weak slabs cannot trap sufficient hot mantle before being drained by neighboring ordinary plumes.

[36] We offer an explanation as to why slab viscosity, or stiffness, is a major factor in determining the plume buoyancy. The small-scale convection beneath slabs is actually akin to stagnant-lid convection. Stagnant-lid convection has a cold, effectively stagnant lid on the top of the convection cell due to the very large viscosity contrast between the lid and convection cell. Numerical study using Newtonian viscosity shows that stagnant-lid convection occurs when the viscosity contrast, $\Delta\eta$, exceeds 10^4 [*Solomatov*, 1995], and $\Delta\eta$ in our models is $10^5 \sim 10^6$. In stagnant-lid convection, the nondimensional temperature at the core of the convection cell is $1 - 1/\ln(\Delta\eta)$ and is independent on the size of the cell. An examination of the temperature of the convection cells at different times in different models confirms this prediction. Since buoyancy is proportional to temperature and volume, and temperature is a constant, when the convection cell erupts, the plume buoyancy is solely determined by the size of the plume (essentially the plume head since the volume of the conduit is small). *Davies* [1993] used a simple

calculation to estimate the radius of a plume head, a, when it rises from a low viscosity basal layer. He found that $a = (\eta_a/\eta_b)^{1/3}h$, where η_a is the viscosity of the ambient fluid, η_b is the viscosity of the basal layer, and h is the thickness of the basal layer. So the volume of the plume head is $\pi h^2(\eta_a/\eta_b)^{2/3}$. In our models, h and η_b are the height and viscosity of the convection cell, which are more or less constant. So η_a, the viscosity of the overlaying slab, controls the volume of the plume head, hence the plume buoyancy at eruption. Ordinary plumes are overlain by the mantle, which has a constant viscosity, and have constant buoyancy in all models as a result. The two models with type-3 outcomes have slab viscosities comparable to ambient mantle when plumes erupt from beneath a slab, so the plume buoyancy are the same as ordinary plumes.

[37] We summarize three important features of the dynamics of fine-scale models: (1) plumes preferentially develop on the edge and center of the slab; (2) the TBL in the slab-free area is thinner than that beneath the slab, as a result of frequent plume formation and eruption in the slab-free area; and (3) in models with type-2 outcomes, substantial amounts of hot material can be trapped beneath the slab, leading to mega-plume formation over long periods of time.

[38] Slabs could also have a substantial influence on the heat flux between the mantle and core. For example, the CMB heat flux of model F10 as a function of time and space is shown in Figure 10. The dark red strip on the central right marks the root of an ordinary plume. Near the left margin, the transition from dark red to bright yellow as a function of time corresponds to the transition from pure conduction (Figure 8b) to small-scale convection (Figure 8c) beneath the slab. The small-scale convection is so vigorous that the cold material is entrained into the bottom of the convection cell and gives a very high heat flux. Just before t_e, the heat flux in this region reaches the maximum and is twice as high as compared with the heat flux in the slab-free area at any time. After t_e, the convection cell erupts as a mega-plume, and the heat flux suddenly returns to the normal value. This shows that the heat flux variation associated
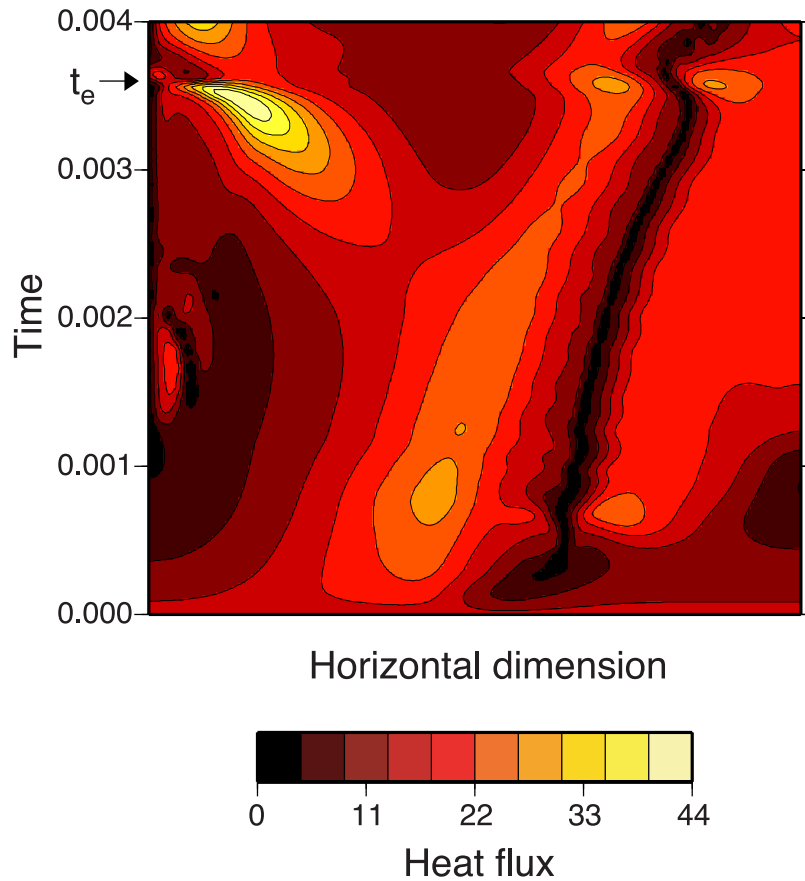
Figure 10. The nondimensional heat flux at the CMB of model F10 as a function of time and horizontal dimension. The eruption time of a mega-plume is also indicated.

with a mega-plume eruption can be very localized in space and abrupt in time, and is substantially larger than those occurring at a normal TBL. All model with type-2 outcomes exhibited these same heat flow characteristics.

4. Discussion

[39] Using models with a high-viscosity lower mantle, a phase transition at 660 km depth, depth-dependent thermal expansivity, and depth-dependent thermal diffusivity, we have shown that slabs always descend to and then come to rest on the CMB. However, by incorporating viable models for evolving plate motions in regional spherical models, we find that although slabs are expected to reach the CMB, they will not necessarily be continuous between the upper and lower mantle. Large gaps in the continuity of slabs are expected as a function of both mantle depth and distance along plate margins because of the time-dependence of plate velocities and plate boundaries. The interaction between slabs and the basal TBL was further investigated by using fine-scale models, and we found this interaction would result in two types of plumes. One, called an ordinary plume, develops on the edge of the slab, drains material from the TBL, and has relatively small buoyancy. The second, called a mega-plume, develops beneath the center of ancient slabs, drains material from recycled slabs, and has relatively large buoyancy. These two types of plumes are significantly different in their location, eruption buoyancy, and geochemical signatures.

[40] It has been suggested that enhanced thermal conductivity will cause slabs to rapidly disappear in the deep mantle. However, even in a model with thermal diffusivity increasing eight-fold with

depth, the slab still reaches the CMB with a significant temperature anomaly. Is a greater increase in thermal diffusivity with depth possible? To estimate the variation in thermal diffusivity, $\kappa = k/\rho C_p$, we need to determine the variation in thermal conductivity, k, density, ρ, and specific heat at constant pressure, C_p, across the mantle. A model of thermal conductivity of the mantle is given by *Hofmeister* [1999], which varies from 2 to 6.7 W/m · K from the top to the bottom of the mantle. The density of the mantle increases from 3500 kg/m^3 to 5500 kg/m^3, according to PREM. Specific heat at constant pressure, C_p, is related to specific heat at constant volume, C_v, via $C_p = C_v(1 + \gamma\alpha T)$, where γ is Grüneisen ratio, α is thermal expansivity, and T is absolute temperature. When T is large, according to the rule of Dulong and Petit, C_v approaches to $3R/m$, where R is the gas constant, and m is mean atomic weight of the mineral. Using $\gamma = 1.2$, $T = \sim1500$ to ~4000 K, $\alpha = 2 \times 10^{-5}$ K^{-1}, and $m = 0.02$ kg/mol, we find C_p changes from 1.3 kJ/kg · K to 1.4 kJ/kg · K. The estimated C_p is compatible with the more rigorous approach of *Akaogi and Ito* [1993b], but they did not extend their calculation to lower mantle conditions. By combining these results, κ has a range of $1.1\sim2.2 \times 10^{-6}$ m^2/s. Although our estimate is subject to a large uncertainty, it does not seem possible to have κ increasing by a factor of 8. So we conclude that thermal diffusion cannot dissipate slabs before they reach the CMB.

[41] At some subduction zones, high seismic velocity anomalies are only found in the upper mantle and deep mantle, but not in the mid-mantle (for example, southern Kuril and India). These gaps in the mid-mantle are often taken as evidence that slabs dissipate before reaching the CMB, disregarding the low resolution of tomography in the mid-mantle. However, we have demonstrated that slabs could be discontinuous when plate velocities are time-dependent. These gaps of slabs in the mid-mantle might result from an abrupt change in plate velocities, i.e., a plate reorganization event [*Fukao et al.*, 2001]. Moreover, changes in convergence history are also likely to play an important role. Examples include the interruption in plate convergence along the Pacific-North America boundary (Figure 6) or the post-Mesozoic re-initiation of subduction that occurred for the Tonga-Kermadec system [*Gurnis et al.*, 2000].

[42] In our 2-D models, the subduction angles are always near vertical, and slabs penetrate the 660-km discontinuity directly. A slab with a shallower subduction angle, resulting from more rapid trench rollback, might become temporarily trapped in the transition zone [*Zhong and Gurnis*, 1995; *Christensen*, 1996; *Ita and King*, 1998]. However, once a slab penetrates the 660-km discontinuity, we find no compelling physical reason why it would not descend to the CMB. The possibility that slabs might be stopped by a change in chemistry or mineralogy cannot be excluded [*Kesson et al.*, 1998; *Kellogg et al.*, 1999].

[43] When slabs reach the CMB, they will have a substantial influence on the dynamics at the CMB. The most pronounced effect is for plumes to be swept onto the edges of slabs. One piece of evidence supporting this possibility is that hot spots correlate with the boundary between high and low seismic velocity regions as determined with tomography at the CMB [*Thorne et al.*, 2001]. Furthermore, *Ni and Helmberger* [2001] and *Luo et al.* [2001] found ULVZs near sharp transitions between high and low seismic velocities beneath South Atlantic and central Pacific. Taken together with a putative link between ULVZ and upwellings [*Williams et al.*, 1998], we suggest that the ULVZs occurring near the high-to-low seismic velocity transitions are a manifestation of ordinary plumes. Because plumes preferentially develop at the edge of slabs, and plumes may give rise to ULVZs, ULVZs are observed at the edge of slabs. However, we cannot overlook the possibility that, although 2-D models always have plumes at slab edges, plumes are more likely to be irregularly distributed around the edges of slabs in 3-D.

[44] Another important effect of slabs at the CMB is their modulation of core-mantle heat flux. The thermal conditions at the CMB are likely to have an important influence on the geodynamo [*Zhang and Gubbins*, 1993; *Glatzmaier et al.*, 1999; *Gibbons and Gubbins*, 2000], though a consensus of whether and how the heat flux variation would
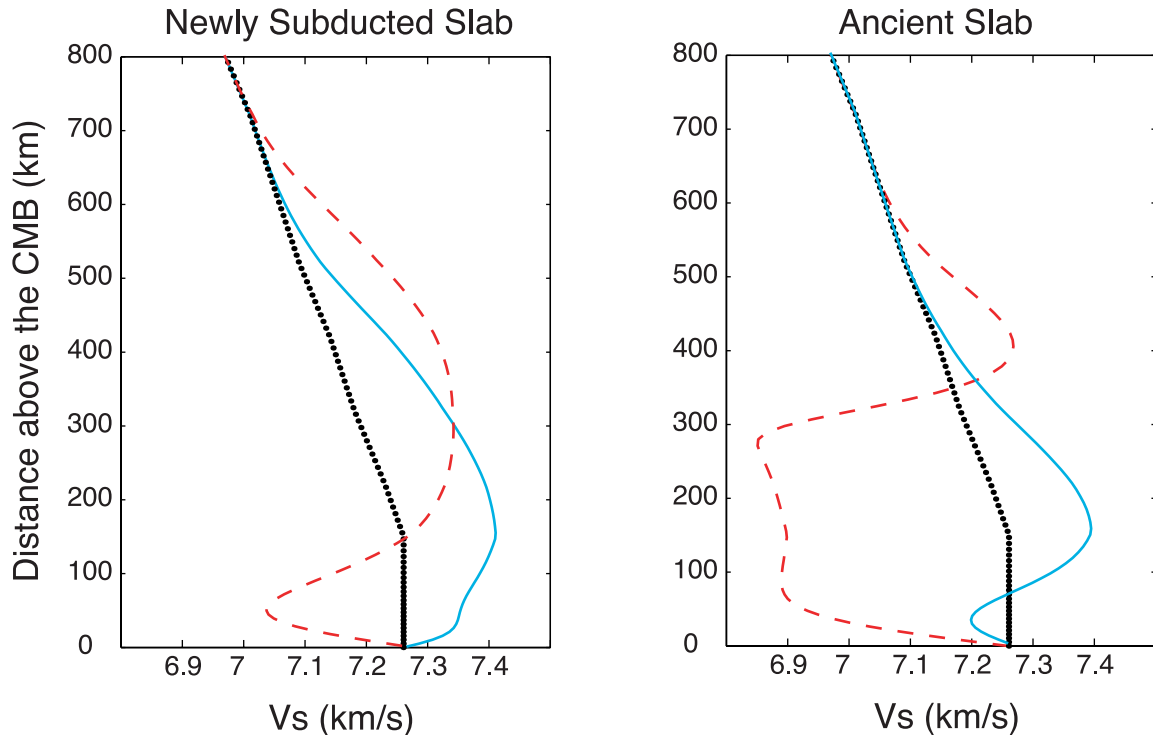
Figure 11. Shear wave velocity profiles above the CMB. Left panel shows profiles from a newly subducted slab (Figure 8b), while right panel shows profiles from an ancient slab (Figure 8c). Red dashed lines indicate profiles taken at the center of slabs, while blue solid lines indicate profiles taken at the edge of slabs. The dotted line is PREM.

affect the geodynamo is not established. *Larson and Olson* [1991] proposed that nearly simultaneous eruptions of several very large plumes from the CMB were responsible for the decrease of magnetic reversal frequency during the Cretaceous. The dramatically enhanced heat flux at the CMB before the formation of mega-plumes provides a viable mechanism to change the magnetic reversal frequency. Additionally, the large buoyancy of mega-plumes in our models is consistent with a huge production of basaltic crust during mid-Cretaceous. These seem to support Larson and Olson's hypothesis. However, with our models, the onset of increased crustal production is likely to lag plume eruption by several tens of million years, due to the time it takes for plumes to rise through the mantle.

[45] The result of fine-scale models showed that those with type-2 outcomes (i.e., mega-plume eruption) occupy a large part of the B_s-S domain (Figure 9). It is natural to ask where the Earth may lay in this space. To answer this question, we need to estimate the possible thickness and temperature anomalies associated with slabs at the CMB. Although we determined a range of thicknesses (~450 to ~650 km) and temperature anomalies (~300° to ~600°C) from our models, we would like to ground-truth our estimate with seismology. An estimate of temperature anomalies of slabs can be obtained from tomography models. Several recent tomography models have RMS-velocity variations $\delta \ln V_p = 0.3\%$ and $\delta \ln V_s = 0.6\%$ over most parts of lower mantle [*Fukao et al.*, 2001]. Recent molecular dynamics simulation on $MgSiO_3$ perovskite leads to $(\partial \ln V_p / \partial T)_p = -1.98 \times 10^{-5}$ K^{-1} and $(\partial \ln V_s / \partial T)_p = -3.78 \times 10^{-5}$ K^{-1} at a depth of 2000 km [*Oganov et al.*, 2001]. Therefore, such a RMS-velocity variation would correspond to a RMS-temperature variation of 150°C. The temperature anomalies in the center of slabs would be much higher than the RMS value, so 150°C gives a lower bound. The regional tomography model in the lowermost mantle beneath southwestern Pacific from *Wysession* [1996] has a maximum
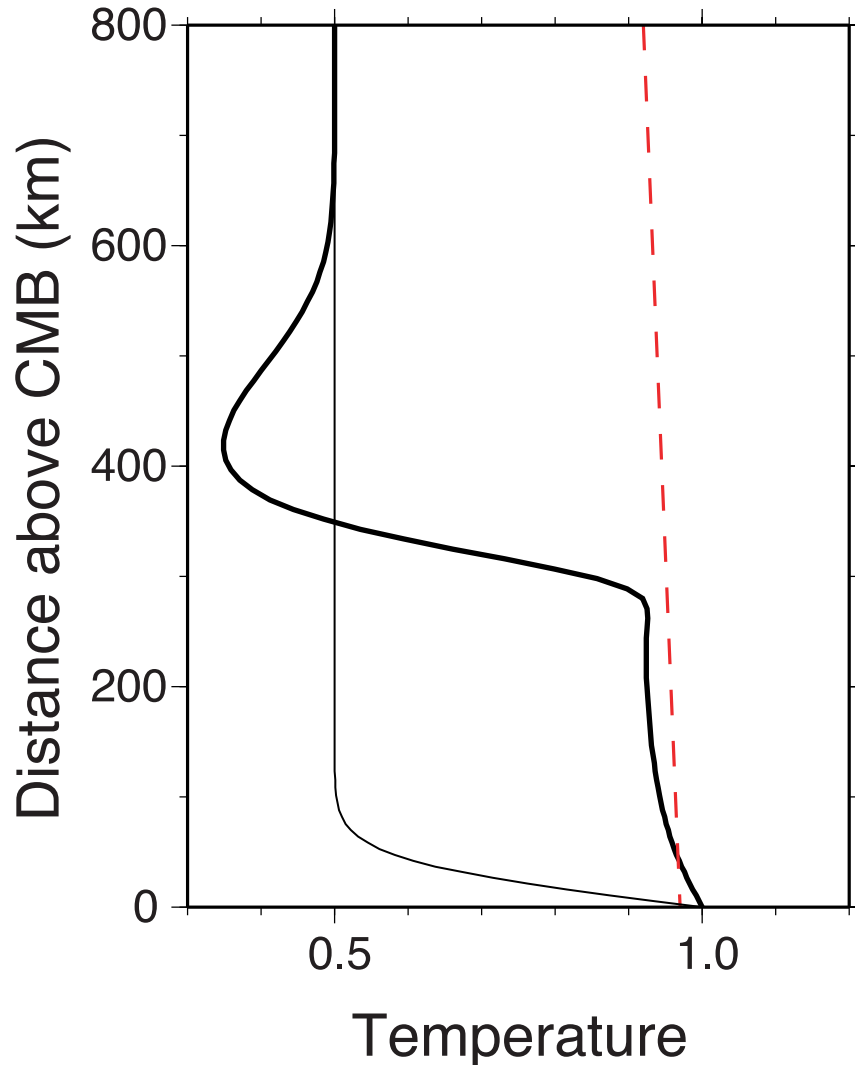
Figure 12. Temperature profiles across the slab (thick line) and across the slab-free area (thin line) along with a hypothetical solidus (dashed line).

$\delta\ln V_p$ = 4%, which is a fairly large velocity variation among tomography models. If we attribute all of the variation to a thermal origin, we get a temperature anomaly of 1000°C as an upper bound. The thickness of slabs cannot be inferred from seismology because tomography tends to smooth mantle structure. A rough estimate of 200 $\sim$ 700 km is used here. Assuming an activation energy of 520 kJ/mol · K and an ambient temperature of 2000 K, the viscosity variation is estimated to be δ_η = 1.1 $\sim$ 13.6. We mark the range of our estimate as the shaded area in Figure 9. Also plotted is the midpoint of our estimate (temperature anomaly 550°C and thickness 450 km). The

shaded area lies almost entirely within the mega-plume regime, suggesting that mega-plumes are relevant to the Earth.

[46] If mega-plumes have occurred in the past, what kind of signature would they have left? Because of their large buoyancies, mega-plumes are likely to penetrate the 660-km discontinuity, reach the surface, and produce hot spots. Since most recycled slab material is incorporated into mega-plumes, we suggest that mega-plumes could be the source of HIMU OIB. The slab would provide a crustal component to the mega-plume while being stiff enough to hold the buoyant plume

at the CMB for a long interval of time. It is an efficient way to keep enriched crustal material from mixing with depleted mantle. We suggest that HIMU hot spots may be found above ancient slabs. This implication is difficult to test since slabs under HIMU hot spots might have been thermally dissipated after nucleating a mega-plume.

[47] On the other hand, if mega-plumes are developing on the CMB today, could we find their signatures? Using a thermal profile from a slab-free area as a reference, we convert thermal profiles to shear wave velocity at the center and edge of slabs of different ages (Figure 11). This conversion is based on temperatures variation only, without including the possible influence of partial melting and variations in chemistry. The thermal structures of slabs produce high seismic velocity anomalies capping low velocity anomalies, and the extent of low velocity anomalies changes substantially with slab location and age. The low velocity anomaly is more profound beneath the center of a slab than beneath a slab edge. An ancient slab is expected to cap a larger low velocity anomaly than a newly subducted slab. The signature of this low velocity anomaly is likely to be compensated by those high velocity anomalies surrounding it. This structure is essentially two-dimensional and may be hidden in previous 1-D studies of D″. Moreover, substantial low velocity anomalies are expected to be found beneath the large volume, seismically fast structures at the CMB. The differential travel time of S and ScS at large epicenter distance (70° to 90°) might be used to detect these regions.

[48] Another possible signature of a developing mega-plume is ULVZ within the geographic center of a slab. We show temperature profiles across a slab and a slab-free area and compare them with a hypothetical solidus (Figure 12). If the solidus intersects the geotherm above the CMB, following the suggestion that ULVZs result from presence of partial melting [*Williams and Garnero*, 1996], our model predicts that a larger degree of partial melting could occur under ancient slabs, and by implication ULVZs could be larger under some old slabs.

[49] The CMB regions beneath Siberia and Caribbean, which have strong high seismic velocity

anomalies and long subduction history, are the most likely places to find developing mega-plumes. The anomalous structure beneath the Caribbean found by *Fisher and Wysession* [2001] and *Wysession et al.* [2001] is a possible candidate in this regard. We suggest a detailed study on these regions to test our predictions.

Acknowledgments

References

Akaogi, M., and E. Ito, Refinement of enthalpy measurement of $MgSiO_3$ perovskite and negative pressure-temperature slopes for perovskite-forming reactions, *Geophys. Res. Lett.*, *20*, 1839–1842, 1993a.

Akaogi, M., and E. Ito, Heat-capacity of $MgSiO_3$ perovskite, *Geophys. Res. Lett.*, *20*, 105–108, 1993b.

Atwater, T., Implications of plate tectonics for the Cenozoic tectonic evolution of western North America, *Geol. Soc. Am. Bull.*, *81*, 3513–3536, 1970.

Atwater, T., and J. Stock, Pacific North America plate tectonics of the Neogene southwestern United States: An update, *Int. Geol. Rev.*, *40*, 375–402, 1998.

Ben-Avraham, Z., and S. Uyeda, Entrapment origin of marginal seas, in *Geodynamics of the Western Pacific-Indonesian Region*, edited by T. W. C. Hilde et al., pp. 91–104, AGU, Washington D. C., 1983.

Chopelas, A., Thermal expansivity of lower mantle phases MgO and $MgSiO_3$ perovskite at high pressure derived from vibrational spectroscopy, *Phys. Earth Planet. Inter.*, *98*, 3–15, 1996.

Christensen, U., Effects of phase-transitions on mantle convection, *Annu. Rev. Earth Planet. Sci.*, *23*, 65–87, 1995.

Christensen, U. R., The influence of trench migration on slab penetration into the lower mantle, *Earth Planet. Sci. Lett.*, *140*, 27–39, 1996.

Creager, K. C., and T. H. Jordan, Slab penetration into the lower mantle beneath the Mariana and other island arcs of the northwest Pacific, *J. Geophys. Res.*, *91*, 3573–3589, 1986.

Davies, G. F., Effect of a low viscosity layer on long-wavelength topography, upper mantle case, *Geophys. Res. Lett.*, *16*, 625–628, 1989.

Davies, G. F., Cooling the core and mantle by plume and plate flows, *Geophys. J. Int.*, *115*, 132–146, 1993.

Davies, G. F., Penetration of plates and plumes through the mantle transition zone, *Earth Planet. Sci. Lett.*, *133*, 507–516, 1995.

Ding, X. Y., and S. P. Grand, Seismic structure of the deep

Kurile subduction zone, *J. Geophys. Res.*, *99*, 23,767–23,786, 1994.

Dziewonski, A. M., and D. L. Anderson, Preliminary reference earth model, *Phys. Earth Planet. Inter.*, *25*, 297–356, 1981.

Fischer, K. M., K. C. Creager, and T. H. Jordan, Mapping the Tonga slab, *J. Geophys. Res.*, *96*, 14,403–14,427, 1991.

Fisher, J. L., and M. E. Wysession, Small scale seismic attenuation within D″, *Eos Trans. AGU*, *82*(47), Fall Meet. Suppl., F1130, 2001.

Fukao, Y., S. Widiyantoro, and M. Obayashi, Stagnant slabs in the upper and lower mantle transition region, *Rev. Geophys.*, *39*, 291–323, 2001.

Garnero, E. J., and D. V. Helmberger, Seismic detection of a thin laterally varying boundary layer at the base of the mantle beneath the central-Pacific, *Geophys. Res. Lett.*, *23*, 977–980, 1996.

Gibbons, S. J., and D. Gubbins, Convection in the Earth's core driven by lateral variations in the core-mantle boundary heat flux, *Geophys. J. Int.*, *142*, 631–642, 2000.

Glatzmaier, G. A., R. S. Coe, L. Hongre, and P. H. Roberts, The role of the Earth's mantle in controlling the frequency of geomagnetic reversals, *Nature*, *401*, 885–890, 1999.

Grand, S. P., R. D. van der Hilst, and S. Widiyantoro, Global seismic tomography: A snapshot of convection in the Earth, *GSA Today*, *7*, 1–7, 1997.

Gurnis, M., J. Ritsema, H. J. van Heijst, and S. Zhong, Tonga slab deformation: The influence of a lower mantle upwelling on a slab in a young subduction zone, *Geophys. Res. Lett.*, *27*, 2373–2376, 2000.

Hager, B. H., Subducted slabs and the geoid—Constraints on mantle rheology and flow, *J. Geophys. Res.*, *89*, 6003–6015, 1984.

Hager, B. H., R. W. Clayton, M. A. Richards, R. P. Comer, and A. M. Dziewonski, Lower mantle heterogeneity, dynamic topography and the geoid, *Nature*, *313*, 541–546, 1985.

Hauck, S. A., R. J. Phillips, and A. M. Hofmeister, Variable conductivity: Effects on the thermal structure of subducting slabs, *Geophys. Res. Lett.*, *26*, 3257–3260, 1999.

Hofmann, A. W., Mantle geochemistry: The message from oceanic volcanism, *Nature*, *385*, 219–229, 1997.

Hofmann, A. W., and W. M. White, Mantle plumes from ancient oceanic crust, *Earth Planet. Sci. Lett.*, *57*, 421–436, 1982.

Hofmeister, A. M., Mantle values of thermal conductivity and the geotherm from phonon lifetimes, *Science*, *283*, 1699–1706, 1999.

Ita, J., and S. D. King, The influence of thermodynamic formulation on simulations of subduction zone geometry and history, *Geophys. Res. Lett.*, *25*, 1463–1466, 1998.

Ito, E., and E. Takahashi, Postspinel transformations in the system Mg_2SiO_4-Fe_2SiO_4 and some geophysical implications, *J. Geophys. Res.*, *94*, 10,637–10,646, 1989.

Kellogg, L. H., B. H. Hager, and R. D. van der Hilst, Compositional stratification in the deep mantle, *Science*, *283*, 1881–1884, 1999.

Kesson, S. E., J. D. F. Gerald, and J. M. Shelley, Mineralogy and dynamics of a pyrolite lower mantle, *Nature*, *393*, 252–255, 1998.

King, S. D., A. Raefsky, and B. H. Hager, Conman—Vector-izing a finite-element code for incompressible 2-dimensional convection in the Earth's mantle, *Phys. Earth Planet. Inter.*, *59*, 195–207, 1990.

Lambeck, K., C. Smither, and P. Johnston, Sea-level change, glacial rebound and mantle viscosity for northern Europe, *Geophys. J. Int.*, *134*, 102–144, 1998.

Larson, R. L., and P. Olson, Mantle plumes control magnetic reversal frequency, *Earth Planet. Sci. Lett.*, *107*, 437–447, 1991.

Lenardic, A., and W. M. Kaula, Tectonic plates, D″ thermal structure, and the nature of mantle plumes, *J. Geophys. Res.*, *99*, 15,697–15,708, 1994.

Lithgow-Bertelloni, C., and M. A. Richards, The dynamics of Cenozoic and Mesozoic plate motions, *Rev. Geophys.*, *36*, 27–78, 1998.

Lowman, J. P., and G. T. Jarvis, Continental collisions in wide aspect ratio and high Rayleigh number two-dimensional mantle convection models, *J. Geophys. Res.*, *101*, 25,485–25,497, 1996.

Luo, S. N., S. D. Ni, and D. V. Helmberger, Evidence for a sharp lateral variation of velocity at the core-mantle boundary from multipathed PKPab, *Earth Planet. Sci. Lett.*, *189*, 155–164, 2001.

Megnin, C., and B. Romanowicz, The three-dimensional shear velocity structure of the mantle from the inversion of body, surface and higher-mode waveforms, *Geophys. J. Int.*, *143*, 709–728, 2000.

Mitrovica, J. X., and A. M. Forte, Radial profile of mantle viscosity: Results from the joint inversion of convection and postglacial rebound observables, *J. Geophys. Res.*, *102*, 2751–2769, 1997.

Moresi, L., M. Gurnis, and S. Zhong, Plate tectonics and convection in the Earth's mantle: Toward a numerical simulation, *Comput. Sci. Eng.*, *2*, 22–33, 2000.

Ni, S. D., and D. V. Helmberger, Horizontal transition from fast to slow structures at the core-mantle boundary: South Atlantic, *Earth Planet. Sci. Lett.*, *187*, 301–310, 2001.

Oganov, A. R., J. P. Brodholt, and G. D. Price, The elastic constants of $MgSiO_3$ perovskite at pressures and temperatures of the Earth's mantle, *Nature*, *411*, 934–937, 2001.

Pankow, K. L., and T. Lay, Constraints on the Kurile slab from shear wave residual sphere analysis, *J. Geophys. Res.*, *104*, 7255–7278, 1999.

Richards, M. A., and D. C. Engebretson, Large-scale mantle convection and the history of subduction, *Nature*, *355*, 437–440, 1992.

Ritsema, J., and H. van Heijst, Seismic imaging of structural heterogeneity in Earth's mantle: Evidence for large-scale mantle flow, *Sci. Progress*, *83*, 243–259, 2000.

Shearer, P. M., and M. P. Flanagan, Seismic velocity and density jumps across the 410- and 660-kilometer discontinuities, *Science*, *285*, 1545–1548, 1999.

Sidorin, I., and M. Gurnis, Geodynamically consistent seismic velocity predictions at the base of the mantle, in *The Core-Mantle Boundary Region*, *Geodyn. Ser.*, vol. 28, edited by M. Gurnis et al., pp. 209–230, AGU, Washington D. C., 1998.

Sidorin, I., M. Gurnis, and D. V. Helmberger, Dynamics of a

phase change at the base of the mantle consistent with seismological observations, *J. Geophys. Res.*, *104*, 15,005–15,023, 1999.

Solomatov, V. S., Scaling of temperature-dependent and stress-dependent viscosity convection, *Phys. Fluids*, *7*, 266–274, 1995.

Thorne, M. S., E. J. Garnero, and S. P. Grand, Seismic evidence for strong chemical heterogeneity at the core mantle boundary as the source of hot spot volcanism, *Eos Trans. AGU*, *82*(47), Fall Meet. Suppl., F1123, 2001.

van der Hilst, R. D., S. Widiyantoro, and E. R. Engdahl, Evidence for deep mantle circulation from global tomography, *Nature*, *386*, 578–584, 1997.

van Keken, P. E., and C. J. Ballentine, Dynamical models of mantle volatile evolution and the role of phase transitions and temperature-dependent rheology, *J. Geophys. Res.*, *104*, 7137–7151, 1999.

Vidale, J. E., and M. A. H. Hedlin, Evidence for partial melt at the core-mantle boundary north Tonga from the strong scattering of seismic waves, *Nature*, *391*, 682–685, 1998.

Wang, Y. B., D. J. Weidner, R. C. Liebermann, and Y. S. Zhao, P-V-T equation of state of $(Mg,Fe)SiO_3$ perovskite—Constraints on composition of the lower mantle, *Phys. Earth Planet. Inter.*, *83*, 13–40, 1994.

Weinstein, S. A., P. L. Olson, and D. A. Yuen, Time-dependent large aspect-ratio convection in the Earth's mantle, *Geophys. Astrophys. Fluid. Dyn.*, *47*, 157–197, 1989.

Williams, Q., and E. J. Garnero, Seismic evidence for partial melt at the base of Earth's mantle, *Science*, *273*, 1528–1530, 1996.

Williams, Q., J. Revenaugh, and E. Garnero, A correlation between ultra-low basal velocities in the mantle and hot spots, *Science*, *281*, 546–549, 1998.

Wysession, M. E., Imaging cold rock at the base of the mantle: The sometimes fate of slabs?, in *Subduction: Top to bottom*, *Geophys. Monogr. Ser.*, vol. 96, edited by G. E. Bebout et al., pp. 369–384, AGU, Washington D. C., 1996.

Wysession, M. E., K. M. Fischer, G. I. Al-eqabi, P. J. Shore, and I. Gurari, Using MOMA broadband array ScS-S data to image smaller-scale structures at the base of the mantle, *Geophys. Res. Lett.*, *28*, 867–870, 2001.

Zhang, K., and D. Gubbins, Convection in a rotating spherical fluid shell with an inhomogeneous temperature boundary-condition at infinite Prandtl number, *J. Fluid Mech.*, *250*, 209–232, 1993.

Zhong, S., and M. Gurnis, Mantle convection with plates and mobile, faulted plate margins, *Science*, *267*, 838–843, 1995.

Zhong, S., and M. Gurnis, Dynamic interaction between tectonics plates, subducting slabs, and the mantle, *Earth Interact.*, *1*, 1997. (Available at http://EarthInteractions.org)